science.sciencemag.org/cgi/content/full/science.aay8015/DC1

Supplementary Materials for

Structural basis for strand transfer inhibitor binding to HIV intasomes

Dario Oliveira Passos[1]*, Min Li[2]*, Ilona K. Jóźwik[1], Xue Zhi Zhao[3], Diogo Santos-Martins[4], Renbin Yang[2], Steven J. Smith[3], Youngmin Jeon[1], Stefano Forli[4], Stephen H. Hughes[3], Terrence R. Burke Jr.[3], Robert Craigie[2], Dmitry Lyumkis[1]†

†Corresponding author. Email: dlyumkis@salk.edu

Published 30 January 2020 on *Science* First Release
DOI: 10.1126/science.aay8015

This PDF file includes:

Materials and Methods

HIV-1 CSC intasome assembly and purification

Sso7d-integrase was overexpressed in *Escherichia coli* BL21 (DE3) and purified as previously described (*4*). Briefly, His tagged Sso7d-IN was expressed in *E. coli* BL21 (DE3) and the cells were lysed in buffer containing 20 mM Hepes pH 7.5, 10% glycerol, 2 mM 2-mercaptoethanol, 20 mM imidazole and 1M NaCl. The protein was purified by nickel-affinity chromatography and the His-tag was removed with thrombin. Aggregated protein was removed by gel filtration on a Hiload 26/60 Superdex-200 column (GE Healthcare) equilibrated with 20 mM Hepes pH 7.5, 10% glycerol, 2 mM DTT and 1M NaCl. The double-stranded vDNA substrate was prepared by annealing the following oligonucleotides:

5'-AGCGTGGGCGGGAAAATCTCTAGCA-3'

5'-ACTGCTAGAGATTTTCCCGCCCACGCT-3'

HIV-1 CSC intasome preparations were assembled as previously described for strand transfer complex STC intasomes (*4*), except 50 μM INSTI was present in the reaction mix, and incubation was carried at 30°C for 60 min. HIV-1 INSTI bound CSC intasomes were purified by Ni-affinity chromatography and two subsequent steps of size exclusion chromatography (SEC). 50 μM of the selected INSTI was added to the intasomes after every step of purification. Briefly, the mixture was first loaded onto a HisTrap HP column (GE Healthcare) previously equilibrated with 20 mM Tris-Cl pH 8.0, 5 mM 2-mercaptoethanol, 5.0 mM $MgCl_2$, 0.5 M NaCl, and 20% (w/v) glycerol. Intasomes were eluted with a linear gradient of 0 mM to 500 mM imidazole in the same buffer. Intasome-containing fractions were combined and concentrated with Amicon Ultra-15 (Ultracel-100k) centrifugal filter. Large CSC aggregates were then removed by gel filtration on a Superose

6 Increase 10/300 GL column (GE Healthcare) equilibrated with 20 mM Bis-Tris pH 6.2, 0.5 mM TCEP, 600 mM NaCl, 5.0 mM $MgCl_2$, and 10% (w/v) glycerol. Pooled intasomes were concentrated prior to TSKgel UltraSW Aggregate HPLC (Tosoh Bioscience) size exclusion chromatography in 20 mM Bis-Tris pH 6.2, 0.5 mM TCEP, 550 mM NaCl, 5mM $MgCl_2$, and 6% (w/v) glycerol. Intasomes fractions corresponding to single CSCs were pooled and the selected INSTI was added to 50 μM. CSCs were concentrated to 0.2 mg/mL for structural studies using cryo-EM. Apo CSCs were prepared in essentially the same way, except $MgCl_2$ and INSTI were substituted by 5.0 mM $CaCl_2$, and $MgCl_2$ was omitted in all purification buffers.

Chemical Materials

BIC was purchased from a commercial source [Cat. no. PBLJ8958, PharmBlock Sciences (Nanjing), Inc.]. Compounds **4d, 4c,** and **4f** were synthesized as previously reported (*19*).

Activity assays

Apo CSC intasomes were assembled with vDNA with a 6-FAM (Fluorescein) label added to the 5′ end of the joining (transferred) strand. Monodisperse 10 nM apo CSC intasomes were incubated with 250 ng of plasmid DNA, pGEM-5zf at 20 mM Hepes, pH 7.5, 20% glycerol, 100 mM NaCl, 10 mM DTT, 4 uM $ZnCl_2$, 5 mM $MgCl_2$ in the absence or presence of 50 μM of the selected INSTI at 37°C for 1 h. The assay was stopped by ethanol precipitation and integration products were separated on 1.5% agarose TBE gel. The gel was visualized by fluorescence scanning of the labeled oligonucleotide (Typhoon 8600, GE Healthcare) followed by ethidium bromide staining.

Cryo-EM specimen preparation for electron microscopy

For each structure determination, 2.5 µL of a sample containing HIV CSC intasomes at ~0.2 mg/ml in SEC buffer (20 mM Bis-Tris pH 6.2, 0.5 mM TCEP, 550 mM NaCl, 5.0 mM $MgCl_2$, and 6% (w/v) glycerol) were applied onto freshly plasma treated (7s, Gatan Solarus plasma cleaner) holey gold UltrAuFoil grid (Quantifoil), adsorbed for 10 seconds and quickly plunged into liquid ethane using manual cryo-plunger operated inside the cold room (~4°C).

Cryo-EM data collection

Data were acquired using the Leginon software (*32*) installed on an FEI/Thermo Fisher Scientific Titan Krios electron microscope at the Scripps Research Institute, operating at 300 keV and using a K2 summit direct electron detector (Gatan) operating in counting mode. A severe preferential orientation was discovered during early attempts at collecting and processing CSC intasome data. For this reason, all micrographs were collected at nominal tilt angles ranging from 20°-40° using previously described protocols (*22*). All data collection statistics are summarized in Table S1.

Electron microscopy data processing

Unless otherwise stated, the same procedures were applied for each individual dataset described in the current work. Movies were corrected for beam-induced movement after the removal of the first 3 sub-frames using Motioncorr2 (*33*), implemented within the Appion platform (*34*). Individual frames were gain corrected, aligned and summed with the application of an exposure filter (*35*). The generated sums (frames 4-80) were used as input for CTF estimation and particle selection. Estimation of the contrast transfer function (CTF) and particle selection were both performed in WARP (*36*). Particles were extracted, and the particle stacks were input into auto 3D classification in cisTEM (*37*). A carefully trained particle picking in WARP allowed us to skip the

2D classification and avoid the exclusion of poorly represented views. Iterative 3D classifications and refinements were performed through Auto-Refine and Manual-Refine tabs in cisTEM using frequencies that did not exceed 80% fractional Nyquist and until no further gains in resolution or map quality were observed. In the first round, two classes were computed, and particles corresponding to the best class were selected for subsequent refinement (fig. S10). A mask comprising the CIC, with outside density filtered to 20Å, was used every last round of the simultaneous classification and refinement. A cycle of per-particle CTF refinement was also performed as the last cycle of each round. Particles corresponding to a class that does not have readily defined features were excluded, and a new round was initiated. This iterative process was performed until no more improvements in quality or resolution of the maps were observed. A final step of beam tilt refinement, using a program provided by Tim Grant (Janelia Research Campus) was applied to all maps. With the exception of **4f**, we observed slight improvements in the quality of the maps and to the global resolution (<0.05 Å). The resolution of **4f** did not improve with beam-tilt refinement, presumably because the residual beam tilt was small within the data. Resolution for all maps was assessed using the conventional Fourier Shell Correlation (FSC) analysis, for both masked and unmasked half-map and map-to-model curves, using the "mtriage" tool implemented within the Phenix package (*38*). The masks for resolution calculation were automatically generated within the mtriage program. Directional resolution volumes were generated using the 3D FSC tool (*22*), whereas the local resolution was generated using sxlocres.py (*39*). As reported previously (*4*), density for Sso7d was not observed within the cryo-EM maps, but is not expected to affect the CIC (fig. S5).

Model building and refinement

The HIV-1 CIC model was built using the initial coordinates of the strand transfer complex (*4*) (PDB 5U1C) or by rigid body docking of individual domains taken from high-resolution crystal structures (PDB 3L3U and 1K6Y) or an NMR structure (1IHV), as appropriate. Individual regions that diverged from the high-resolution crystal structures were adjusted as necessary and/or missing regions were built manually in Coot (*40*). Final models were generated by iterative model building using Coot (*40*) and refinement with phenix.real_space_refine (*38*), using secondary structure restraints. In the last rounds of refinement, ligand coordinates were added to the models. For compound **4f**, ligand coordinates were taken from PDB deposited structure (PDB 5FRO) and restraint files generated using phenix.elbow (*41*). For **BIC** and compound **4d**, the SMILES strings were taken from PubChem, and the ligand coordinates and topology files were obtained from PRODRG2 server (*42*). For **4c**, restraints were generated by phenix.eLBOW, and the coordinates adopted from the structure of **4d** intasome. Due to limited resolution, waters were not placed into the **4c** bound intasome maps. Waters were modeled for the apo, **4d**, **4f**, and **BIC** intasomes. Waters were modeled based on careful inspection of all four maps, guided by the highest resolution structure of **4d** intasome. Waters were placed into their relevant regions if a bump of density was observed in all four independently refined maps. In some instances, the density was weak, but a water was placed based on inspection of the local chemical environment. For the most stable water molecules, these densities directly overlapped across independent maps. In other instances, presumably for the less stable water molecules, the densities were in similar locations and chemical environments, but not necessarily directly overlapping. To quantitatively determine their correspondence to density and to decide which to eliminate in the deposited models, we also assigned Q-values to water molecules (*43*), as shown in fig. S15. All of the water molecules were carefully inspected and cross-validated across different maps. The geometry of the final models

and other validation statistics were reported by Molprobity (*44*). The relevant refinement statistics are summarized in Table S1. High-resolution structural figures were prepared for publication using UCSF Chimera (*45*).

Sequence and structure analysis

To determine sequence alignment and structure conservation, we used the following procedures. Two PDB files representing the CCD domains of the HIV (BIC bound structure) and PFV (DTG bound structure, PDB 3S3M) as found in their chains A were written out in Chimera and supplied to the PDBeFold server (*46*). Superposition resulted in 0.69 Q-score, 1.51 Å root-mean-square deviation and 25% sequence identity between 130 matched residues. For analysis of the conservation of the active site, the structure of HIV CSC with **BIC** bound was superimposed with the structure of the PFV intasome with **DTG** bound (PDB 3S3M), based on the positions of their A chains. Residues within a zone <10 Å away from the bound BIC were selected, noted (43 residues specified in Table S2) and compared with the best structurally-aligning residues in the PFV intasome structure. The occupancy of the 3'-terminal adenine (dA21) conformers was estimated thanks to 'Values at atom positions' option in the UCSF Chimera (*45*).

Quantum Mechanical Calculations

The torsional profiles (fig. S16) were calculated at the M06-2X/6-31+G(d,p) level of theory using Gaussian 09. The bond torsion was scanned in intervals of 10 degrees. At each interval, the torsion angle was fixed at the desired angle while all the other degrees of freedom were allowed to optimize. Electrostatic surface potentials were also calculated at the M06-2X/6-31+G(d,p) level of theory using Gaussian 09. For this calculation, scaffolds A and B (fig. S16) were geometrically

optimized in the anion form, by deprotonating the hydroxyl group. Then, the electrostatic potential was calculated for about 7000 points in the vicinity of the van de Waals surface of the scaffolds. The minimum value is located in the region that coordinates magnesium and is reported in fig. S16.

Cell-based assays

HIV-based viral vectors with either WT or mutant IN were used in single-round infectivity assays to determine the antiviral activity (EC_{50} values) of the compounds, as previously described(*47*). Briefly, VSV-g-pseudotyped HIV was produced by transfections of 293 cells with pNLNgoMIVR$^-$ ΔLUC and pHCMV-g (obtained from Dr. Jane Burns, University of California, San Diego) using the calcium phosphate method. At approximately 6 hrs after the calcium phosphate precipitate was added, 293 cells were washed twice with phosphate-buffered saline (PBS) and incubated with fresh media for 48 hrs. The virus-containing supernatants were then harvested, clarified by low-speed centrifugation, filtrated, and diluted for preparation in antiviral infection assays. On the day prior to the screen, HOS cells were seeded in a 96-well luminescence cell culture plate at a density of 4000 cells in 100 µL of medium per well. On the day of the screen for antiviral activity infection assays, cells were treated with compounds using a range of concentration from 5 µM to 0.0001 µM in 11 serial dilutions, and the cells were incubated at 37^{o}C for 3 hrs. The compounds used to treat cells are indicated in fig. S8. 100 µL aliquots of the virus-stock, diluted to achieve a luciferase signal between 0.2 and 1.5 Relative Luciferase Units (RLUs), containing the appropriate dilutions of the compounds, were added to each well. The cells were incubated at 37^{o}C for 48 hrs. Infectivity was measured by using the Steady-lite plus luminescence reporter gene assay system (PerkinElmer, Waltham, MA). Luciferase activity was measured by adding 100 µL of Steady-lite

plus buffer (PerkinElmer) to the cells, incubating at room temperature for 20 mins, and measuring luminescence using a microplate reader. Antiviral activities were normalized to the infectivity in cells in the absence of compounds. KaleidaGraph (Synergy Software, Reading, PA) was used to perform non-linear regression analysis on the data. EC_{50} values were determined from the fit model.

Vector Constructs

The construction of the mutant INs S153Y, R263K, E138K/Q148K, G140S/Q148H, and G140S/Q148K has been described previously (*26*). To make the new IN mutants, the vector pNLNgoMIVR-ΔENV.LUC, which has been described previously (*25*), was used to produce the new IN mutants used in this study. The IN open reading frame was removed from pNLNgoMIVR-ΔENV.LUC by digestion with KpnI and SalI and resulting fragment was inserted between the KpnI and SalI sites of pBluescript KS+. Using that construct as the wild-type template, we prepared the following HIV-1 IN mutants M50I/R263K, S119R/R263K, T124A/S153Y, M50I/S119R/R263K, V72I/E138K/Q148K, G140S/Q148H/G149A, and L74M/G140S/S147G/Q148K using the QuikChange II XL site directed mutagenesis kit (Agilent Technologies, Santa Clara, CA. The following sense oligonucleotides were used with matching cognate antisense oligonucleotides (not shown) (Integrated DNA Technologies, Coralville, IA) in the mutagenesis:

M50I, 5′-CAGCTAAAAGGGGAAGCCATTCATGGACAAGTAGACTGT-3′;

V72I, 5′- ACACATTTAGAAGGAAAAATTATCTTGGTAGCAGTT-3′;

L74M, 5′-TTAGAAGGAAAAGTTATCATGGTAGCAGTTCATGTAGCC-3′;

S119R, 5′- GTACATACAGACAATGGCCGTAATTTCACCAGTACTACA-3′;

T124A, 5′- GGCAGCAATTTCACCAGTGCTACAGTTAAGGCCGCCTGT-3′;

S147G 5′- ATTCCCTACAATCCCCAAGGTCGTGGAGTAATAGAATCT-3′;

G149A, 5′- TACAATCCCCAAAGTCAAGCAGTAATAGAATCTATGAAT-3′.

The IN mutants M50I/R263K, S119R/R263K, T124A/S153Y, and M50I/S119R/R263K (shown in fig. S8), were made as follows: The M50I/R263K and S119R/R263K IN mutants were made using the previously generated R263K mutant and the M50I and S119R oligonucleotides were employed to introduce the second mutations. The IN mutant T124A/S153Y was constructed using the previously made S153Y IN mutant, with the appropriate T124A oligonucleotides being used to add the second mutation. The IN mutant M50I/S119R/R263K was made using the aforementioned IN mutant M50I/R263K with the S119R oligonucleotides being used to add the third mutation. The IN mutant V72I/E138K/Q148K was made using the previously generated IN mutant E138K/Q148K and the appropriate oligonucleotides for V72I, to add the third mutation. The IN mutant G140S/Q148H/G149A was made using the previously constructed IN mutant G140S/Q148H and the appropriate oligonucleotides for G149A to add the third mutation. The IN mutant L74M/G140S/S147G/Q148K was made using the previously generated IN mutant G140S/Q148K and appropriately listed oligonucleotides for L74M and S147G, respectively, to add the third and fourth mutations. The DNA sequence of each construct was determined. The mutated IN coding sequences from pBluescript KS+ were then subcloned into pNLNgoMIVR-ΔEnv.LUC (between the KpnI and SalI sites) to produce mutant HIV-1 constructs, which were also checked by DNA sequencing.

Supplementary Text

Supplementary Note 1: Electrostatic potential of the 4-amino group within the naphthyridine core

The strength of magnesium coordination from the ligands is modulated by the electrostatic potential on their surface. Density functional theory calculations show that the electron-donating amino group on the naphthyridine affects the electrostatic potential in a measurable way (increasing from -143 to -146.8 atomic units). This difference would increase the strength of the magnesium coordination and contribute to the binding affinity.

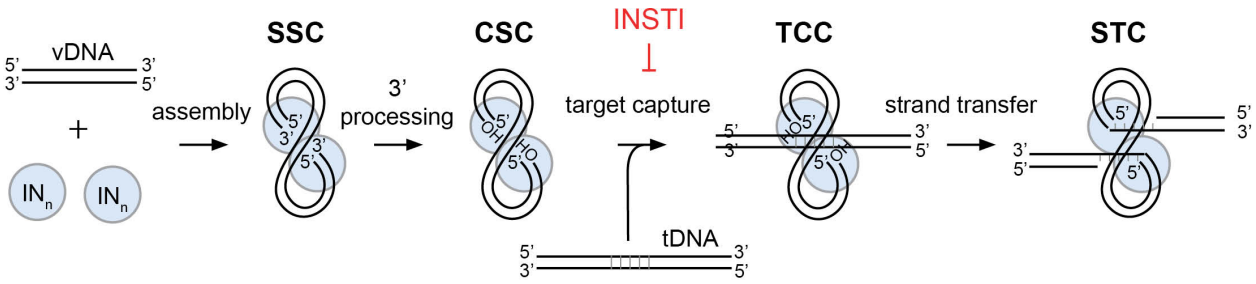

Fig. S1. Intasome assembly scheme. Under specific biochemical conditions, an oligomer of IN proteins will assemble on the ends of vDNA to form the stable synaptic complex (SSC). IN then cleaves two nucleotides from the 3′ ends of vDNA, forming the cleaved synaptic complex (CSC) that exposes the conserved free 3′-OH groups of the catalytically competent CA dinucleotides. CSC intasomes can capture target DNA (tDNA) to form the target capture complex (TCC), which will rapidly catalyze strand transfer to form the post-catalytic strand transfer complex (STC) in which the tDNA and the integrated vDNA are still bound to the intasome. INSTIs specifically bind to CSC intasomes and prevent the formation of the TCC(*6*), inhibiting catalysis.

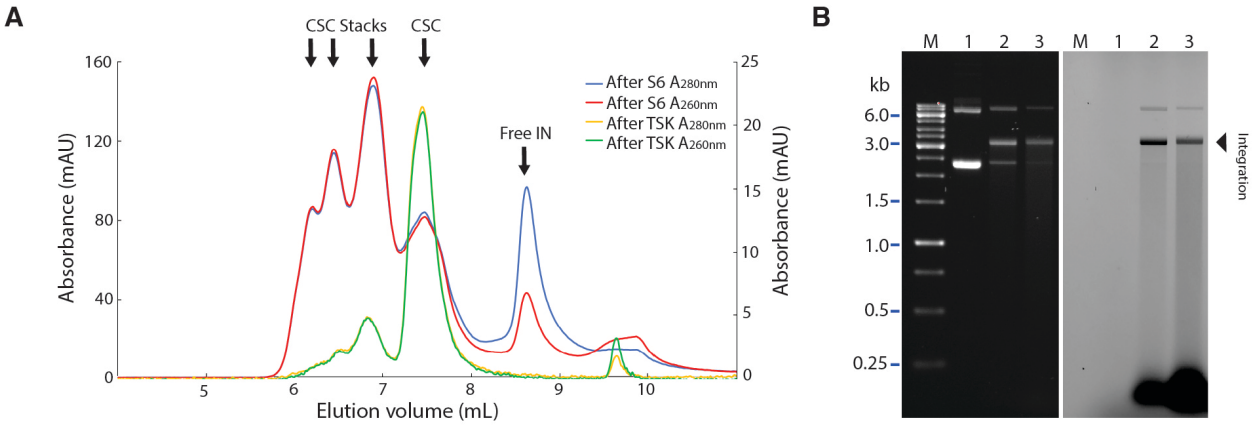

Fig. S2. CSC intasome purification and functional analysis. **(A)** Apo CSC intasomes were first separated on a Superose 6 column. After the initial separation, partially purified apo CSC intasomes from the Superose 6 purification were further subjected to a size exclusion purification by TSKgel Ultra HPLC column (red and blue). The profile showed a residual amount of size heterogeneity. The larger species were identified as intasome stacks (see fig. S4). Intasomes that eluted between 7.0 and 8.0 mL were collected for another round of size exclusion to verify their purity and stability. Reinjection of the eluted complexes onto the same TSKgel Ultra HPLC column (yellow/green curve) showed that most of the larger intasome stacks were removed for subsequent structural studies. **(B)** Intasome activity assay post-TSKgel purification. Integration products were separated on an agarose gel and visualized by ethidium bromide staining (left) and fluorescence scanning (right). Only labeled oligonucleotides are detected with fluorescence scanning. Lane 1, intasomes were omitted from reaction; lane 2 and 3, 10 nM and 20nM of apo intasomes were added into the reaction mixtures, respectively.

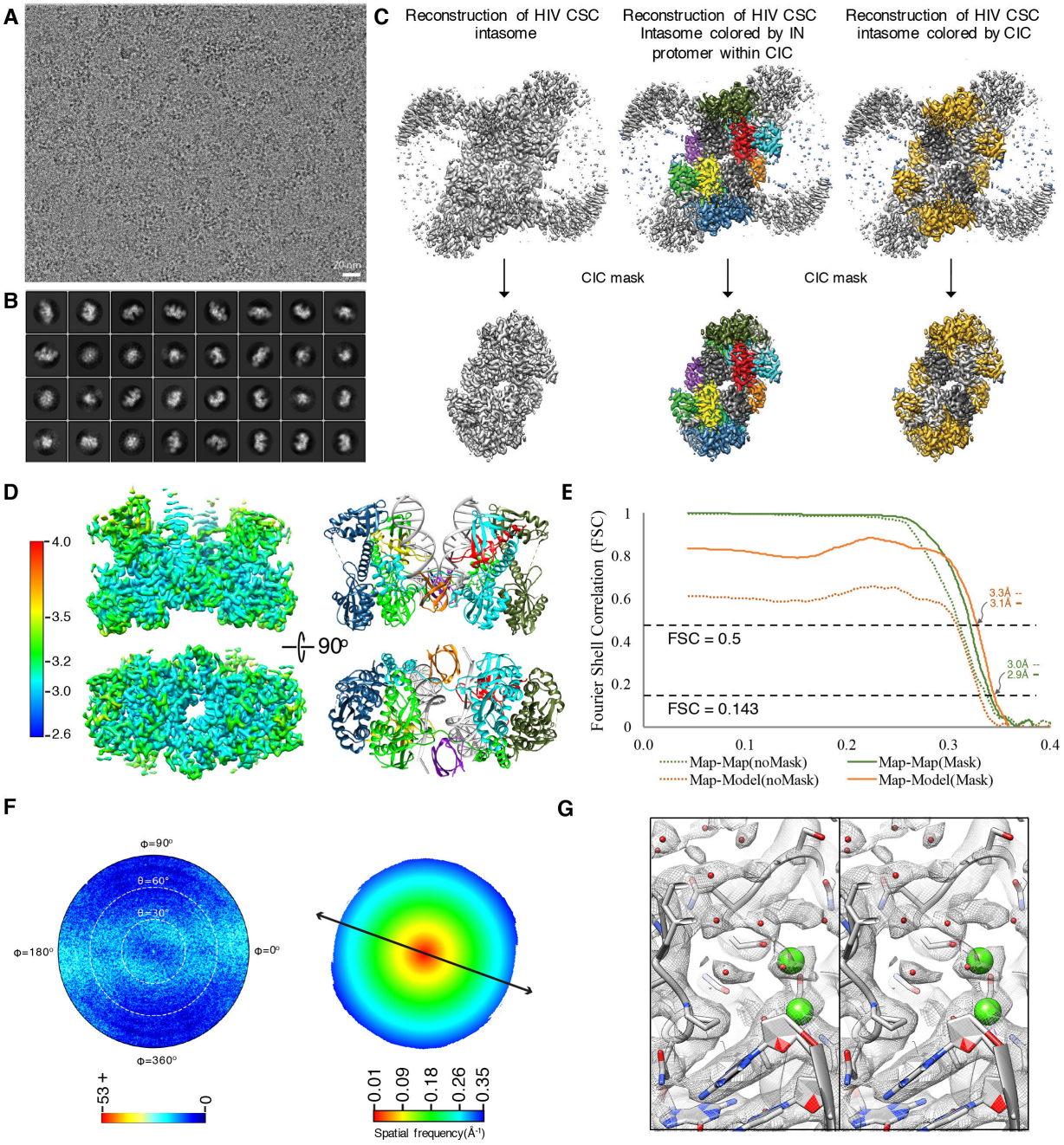

Fig. S3. Cryo-EM structure determination and validation of the apo form of HIV CSC. (**A**) Representative cryo-EM micrograph of HIV apo CSC, taken at -2.15 µm defocus (scale bar, 20nm). (**B**) Selected 2D class averages. (**C**) Reconstructions of the HIV CSC intasome (top) and masked by CIC (bottom). Reconstructions at top reveal a dodecameric configuration of protomers. Maps are colored to either highlight the 6+2 different protomers found within the masked region

(center) or the 6 protomers comprising the HIV CIC (right). Colors refer to: cyan and dark green – dimer 1; light green and dark blue – dimer 2; purple and orange – flanking protomers; yellow and red – distal protomers that are not part of the CIC and have only been observed in lentiviral intasomes. (**D**) Reconstruction of the apo CSC intasome colored by local resolution (left), and atomic model colored by the eight protomers (right). Side and bottom views are displayed on the top and bottom, respectively, for both map and model. The highest resolution is in the active site and reached ~2.7 Å. (**E**) Half-map and map-to-model Fourier Shell Correlation (FSC) curves for masked and unmasked maps. Cutoffs for 0.143 and 0.5 are shown. (**F**) Euler angle distribution plot describing the relative particle orientations contributing to the final refined map (values refer to particle count) and the 3DFSC isosurface plot showing the resolution range of the map for the least favorable cross-sectional view (values refer to resolution). Arrow indicates the direction of preferred orientation (Z-resolution with respect to the electron beam). (**G**) Stereo view of the apo map and model highlighting the catalytic core, where INSTIs bind. The 3′-adenine 21 (dA21) is positioned in its stacking conformation with the penultimate nucleotide cytosine 20 (dC20). Ca^{2+} ions are in green, waters in red.

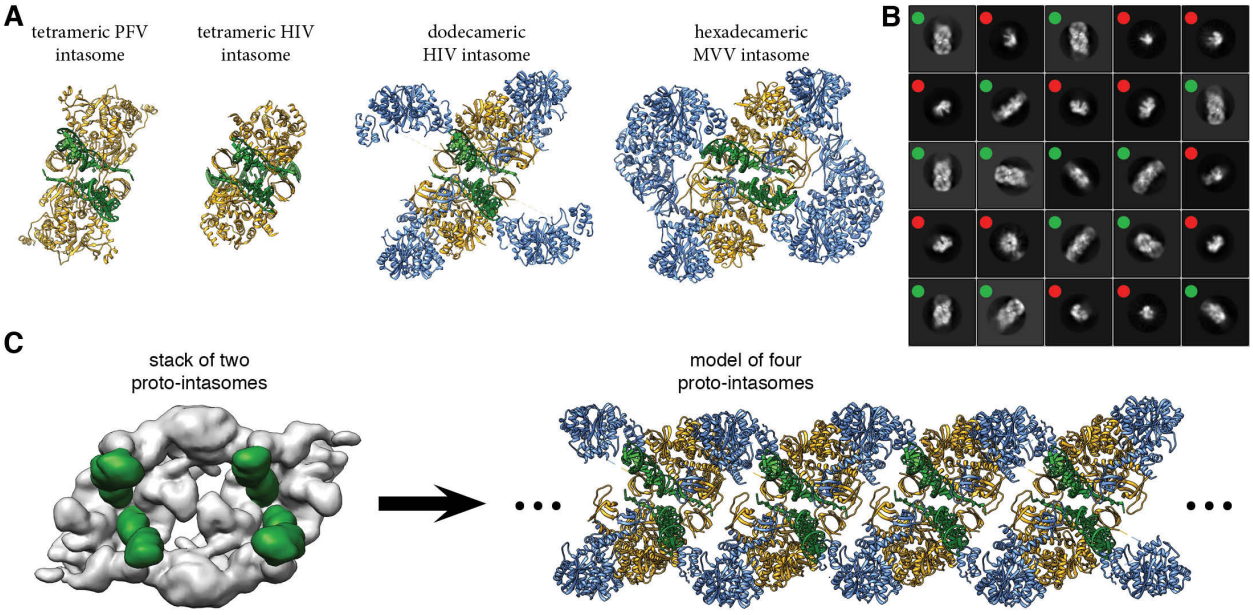

Fig. S4. Lentiviral intasomes assemble to form distinct species *in vitro*. (A) Comparison of the prototype foamy virus (PFV) tetrameric intasome (*6*), the HIV tetrameric and dodecameric intasomes (*4*), and the Maedi Visna Virus (MVV) hexadecameric intasome (*7*). Colors refer to: DNA, green; CIC, yellow; remaining IN protomers, blue. The CIC is highlighted for all species. **(B)** 2D class averages from the current work collected from a dataset prior to passing the sample through the TSKGel HPLC columns and removing the majority of the large species. The large species are indicated by green dots and small species (which are dodecameric CSC intasomes) indicated by red dots. **(C)** The large species could be independently selected, refined, and reconstructed using single-particle analysis, revealing a map with multiple sets of vDNA (left). Rigid body docking of IN components, colored by CIC, shows that these oligomers correspond to "proto-intasome" stacks (right), which are not biologically relevant due to the presence of multiple copies of vDNA, but nonetheless assemble a similar CIC, due to interface conservation. Intasome stacks were not further pursued, because we were able to isolate monodisperse CSCs.

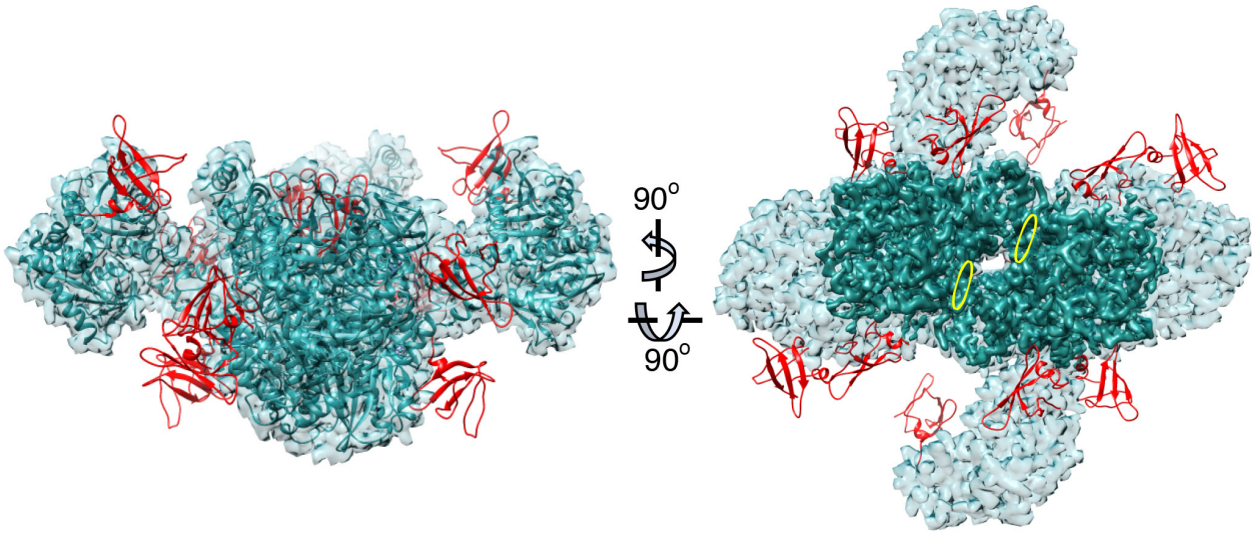

Fig. S5. Putative position of the Sso7d fusion domain within Sso7d HIV intasomes. Molecular surface views of a dodecameric HIV intasome assembly. The CIC is dark. Putative locations of the Sso7d fusion domain, which is invisible within experimental cryo-EM density maps (likely due to flexibility conferred by the glycine linkers), are colored red. Notably, these locations are not expected to interfere with the CIC, where INSTIs bind.

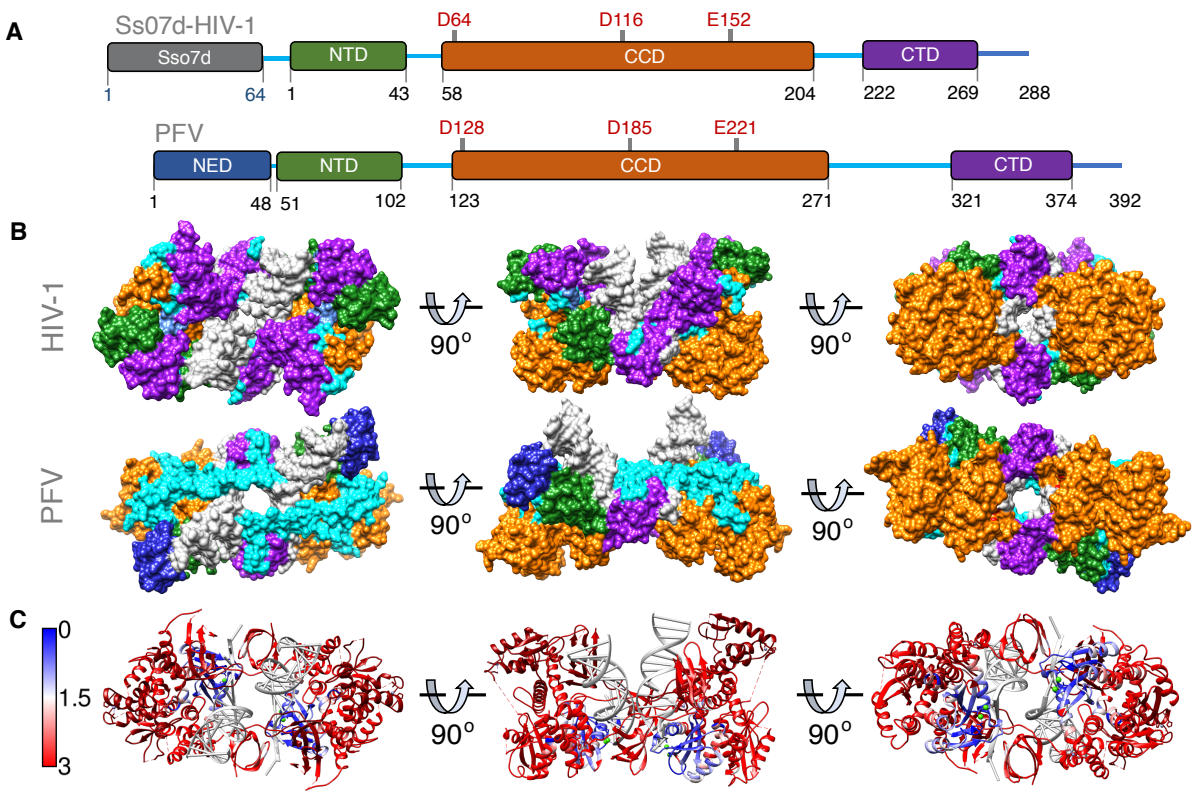

Fig. S6. Differences between PFV and HIV intasome CICs. (**A**) Domain organization of Sso7d-HIV and PFV IN. Conserved domains are colored as following: green, NTD; orange, CCD; purple, CTD; cyan, linkers. (**B**) Domain organization within HIV and PFV CICs, shown in a molecular surface representation, colored as in A. (**C**) Atomic model of the HIV intasome CIC, colored by RMSD corresponding to a structure-based alignment with the PFV intasome CIC. The orientation of the models matches those in B. The vDNA is in gray and the regions of the HIV atomic model that are missing in PFV intasomes are colored dark red. RMSD scale ranges from: 0 Å (blue), 1.5 Å (white) and 3 Å (red).

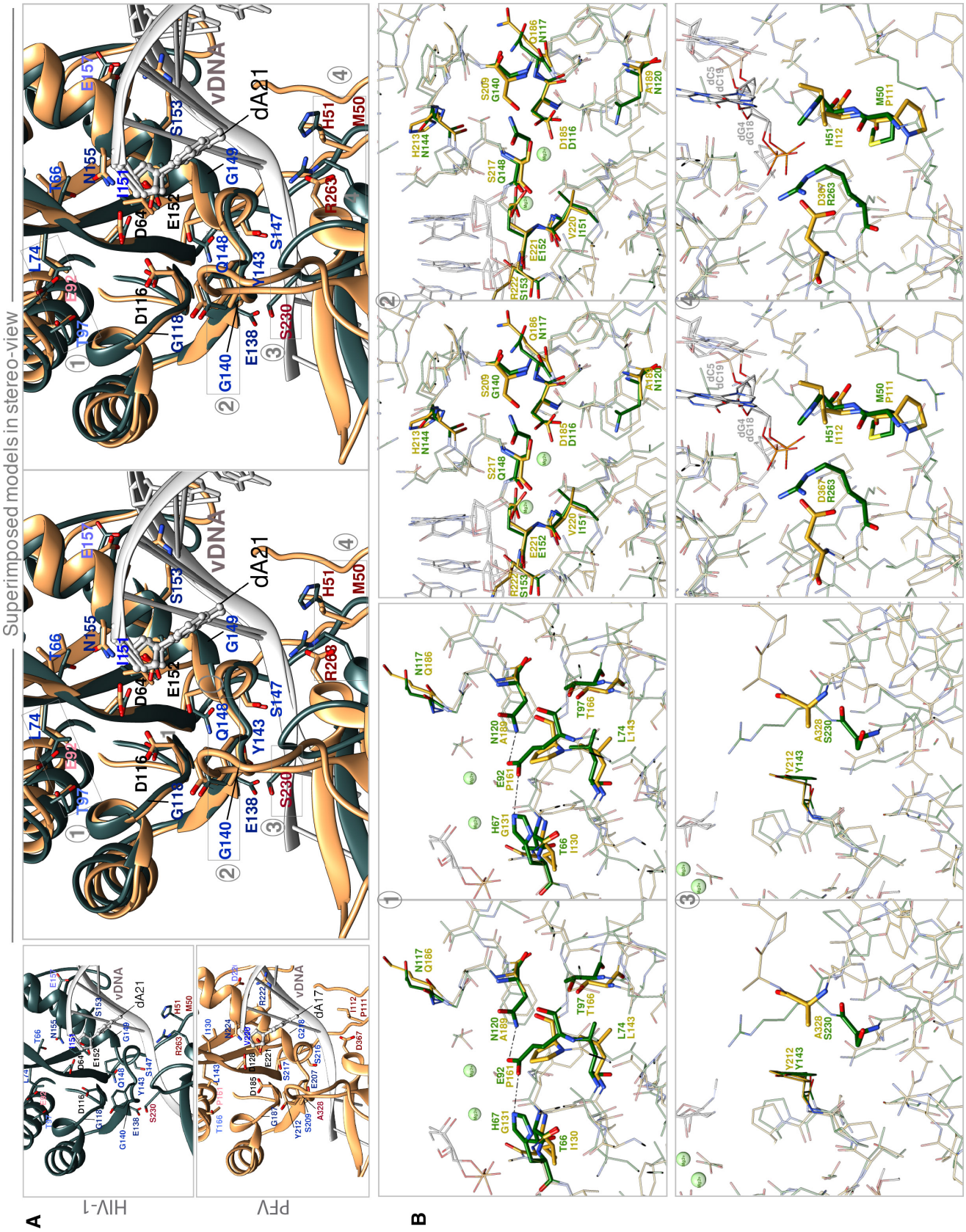
Superimposed models in stereo-view
A
HIV-1
PFV
B
vDNA
dA21
dA17
T97
E92
L74
T66
N155
I151
D64
E152
S153
E157
D116
G118
Q148
Y143
S147
G140
E138
S230
R268
G149
H51
M50
R263
N117
Q186
N120
A189
H67
G131
T66
I130
E92
P161
T97
T166
L74
L143
S209
G140
H218
N144
S217
Q148
D185
D116
V220
I151
E221
E152
R222
S153
A189
N120
Y212
Y143
A328
S230
dC5
dC19
dG4
dG18
H51
I112
M50
P111
D367
R263

Fig. S7. Differences between PFV and HIV intasome in the active site. (**A**) The active site of the HIV (green, top panel) and PFV (gold, bottom panel) apo intasomes, displayed with the same orientation as in Fig. 1C. Residues associated with INSTI resistance are highlighted for HIV and their corresponding residues in PFV IN. Stereo-view of the superimposed HIV and PFV intasome active sites are displayed. Numbers refer to regions of interest containing viral resistant variants not conserved between HIV and PFV (**B**) Close-up stereo views of resistant variants (bold) and surrounding regions indicated in panel A. Strong interactions are represented by dashed lines. Alignment of the two regions was performed on the IN CCD.

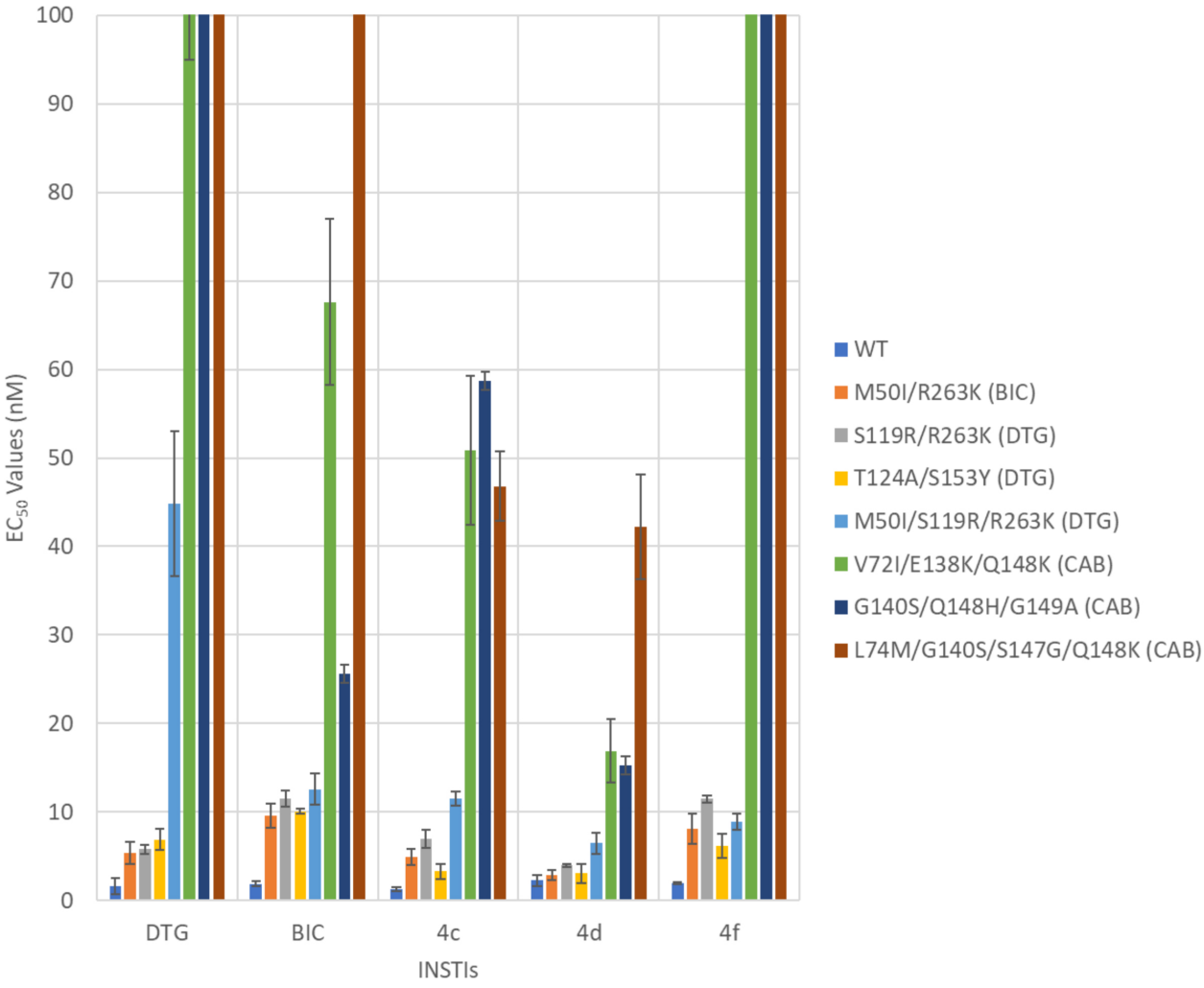

Fig. S8. Comparison of antiviral potencies against a panel of INSTI-resistant mutants selected in vitro. The EC_{50} values were determined for the clinically relevant INSTIs (**DTG** and **BIC**) and our compounds using vectors that carry INSTI-resistant double, triple, and quadruple mutants in a single-round infection assay, shown up to a maximum concentration of 100 nM. The compounds used for treating cells and generating drug resistant variants are indicated for each set of mutants. The error bars represent standard deviations of independent experiments, n=3.

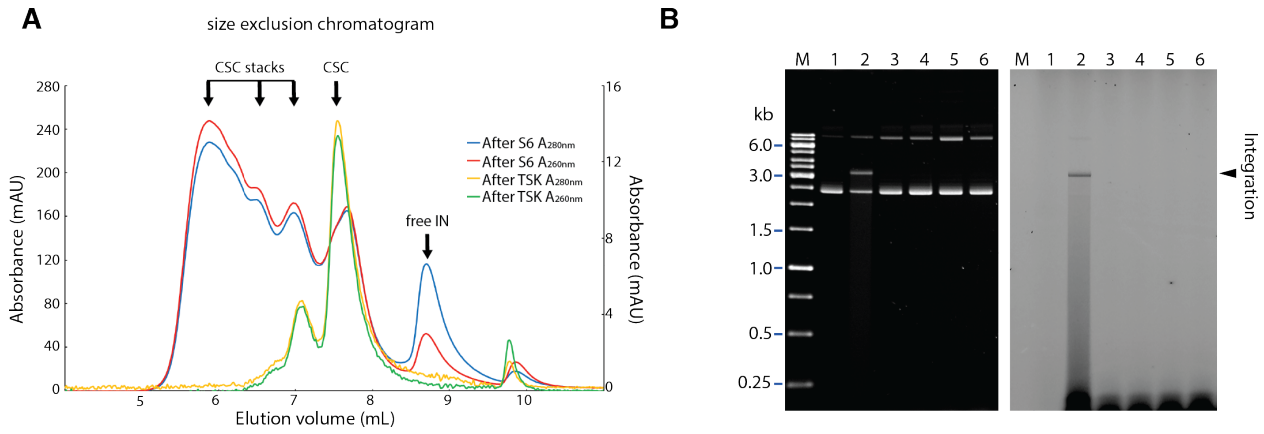

Fig. S9. INSTI-bound CSC intasome purification and functional analysis. (A) Intasomes bound to **BIC** were first separated on a Superose 6 column. After the initial separation, partially purified intasomes from the Superose 6 purification were further subjected to a size exclusion purification by TSKgel Ultra HPLC column (red and blue). Intasomes that eluted between 7.0 and 8.0 mL were collected for another round of size exclusion to verify their purity. Similar to apo intasomes, reinjection of the eluted complexes onto the same column (yellow/green curve) yielded $CSC_{\mathbf{BIC}}$ complexes suitable for structural studies. Profiles for intasomes that contained compounds **4d** and **4f** looked similar to the **BIC**-containing intasomes. **(B)** Intasome activity assay. Apo intasomes were isolated and inhibited with INSTIs. Integration products were separated on an agarose gel and visualized by EB staining (left) and fluorescence scanning (right). Lane 1, intasome was omitted from reaction; lane 2, 10 nM apo intasome was added into the reaction mixture, respectively; lane 3-6, reactions were carried out in the presence of 10 nM intasome and 0.05 mM of the respective inhibitor, **BIC, 4d, 4f,** and **4c**.

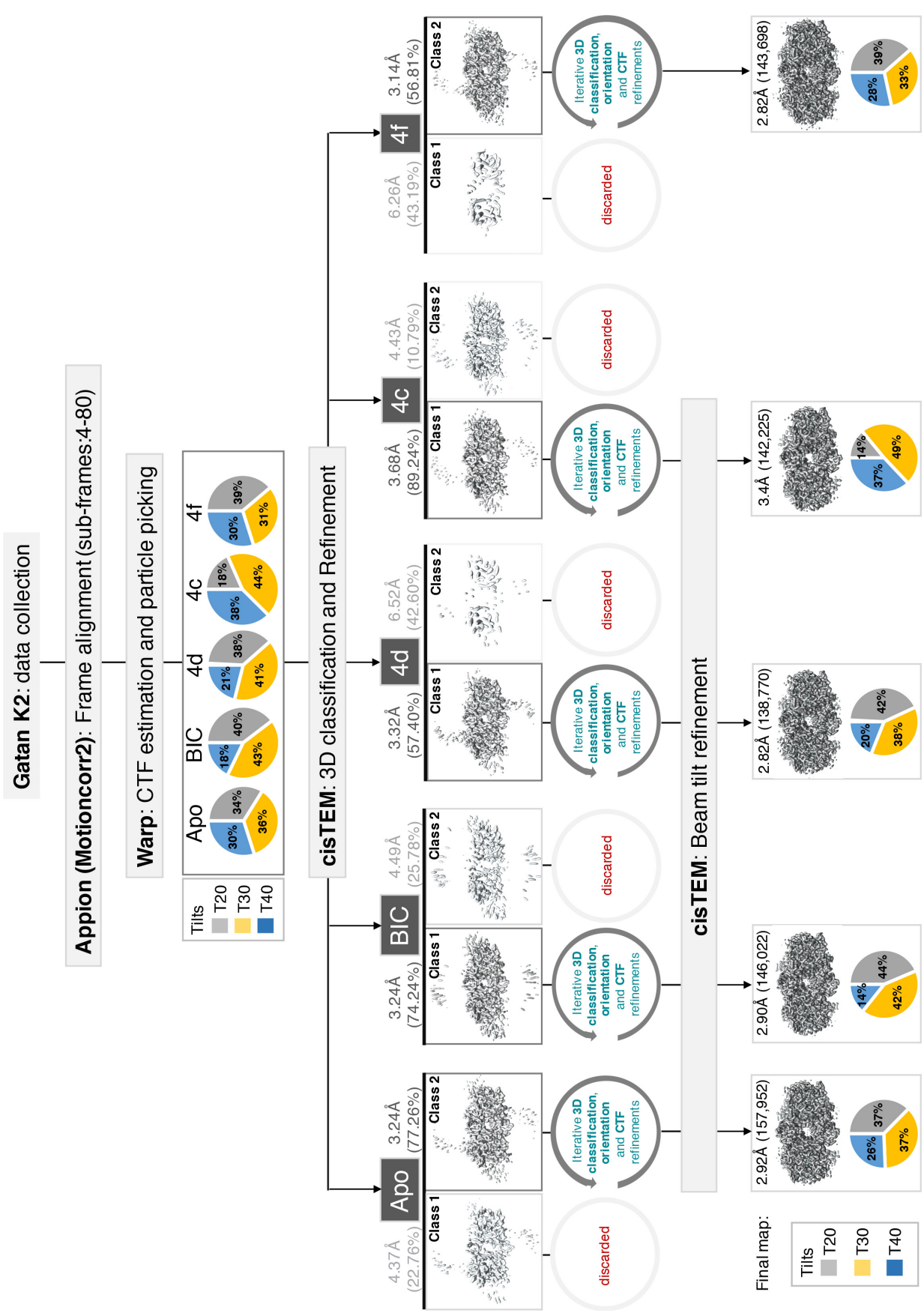
Gatan K2: data collection
Appion (Motioncorr2): Frame alignment (sub-frames:4-80)
Warp: CTF estimation and particle picking
Apo
BIC
4d
4c
4f
Tilts
T20
T30
T40
30%
34%
36%
18%
40%
43%
21%
38%
41%
38%
44%
18%
30%
31%
39%
cisTEM: 3D classification and Refinement
Apo
BIC
4d
4c
4f
4.37Å (22.76%)
3.24Å (74.24%)
4.49Å (25.78%)
3.32Å (57.40%)
6.52Å (42.60%)
3.68Å (89.24%)
4.43Å (10.79%)
6.26Å (43.19%)
3.14Å (56.81%)
Class 1
Class 2
discarded
Iterative 3D classification, orientation and CTF refinements
cisTEM: Beam tilt refinement
2.92Å (157,952)
2.90Å (146,022)
2.82Å (138,770)
3.4Å (142,225)
2.82Å (143,698)
Final map:
Tilts
T20
T30
T40
26%
37%
37%
14%
44%
42%
20%
42%
38%
14%
37%
49%
28%
39%
33%

Figure S10. Image processing strategy for the high-resolution intasome maps. All datasets were collected using tilts (T20 = 20°, T30 = 30°, T40 = 40°) with numbers defined in Table S1. Movies were corrected for beam-induced movement after the removal of the first 3 sub-frames using Motioncorr2, implemented within the Appion platform. The generated sums (4-80) were used for CTF estimation and particle picking in WARP. The initial distribution of particles from different tilted datasets is shown in the upper pie plot. WARP outputs were converted into cisTEM inputs. Iterative 3D classifications and refinements were performed through Auto-Refine and Manual-Refine tabs in cisTEM. 3D Classification and refinements were performed until no further gains in resolution or map quality were observed. A final step of beam tilt refinement using a program provided by Tim Grant (Janelia Research Campus) was applied to all maps (the **4f** complex did not benefit from this approach). The contribution of the tilted particles for the final maps is represented by the pie plots below.

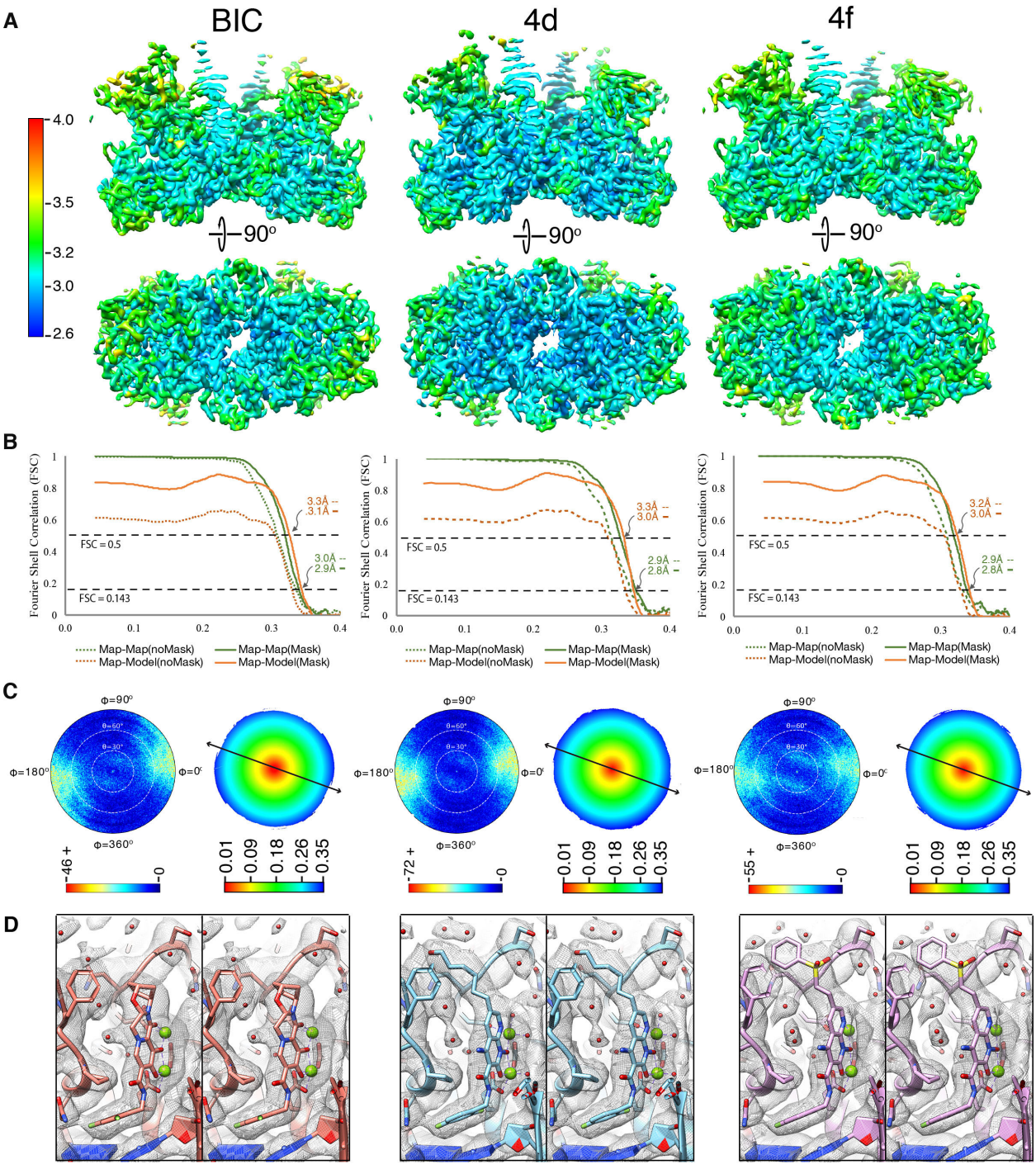

Fig. S11. Cryo-EM structure determination and validation of compounds BIC, 4d, and 4f bound to the HIV CSC intasome. (**A**) Local resolution estimates for each map, colored in Chimera. Side and bottom views of the reconstructions are shown. (**B**) FSC curves for half-map and map-to-model, both masked and unmasked, showing both FSC cutoffs 0.143 and 0.5. (**C**)

Euler angle distribution plots describing the relative particle orientations contributing to the final refined maps (values refer to particle count) and the 3D FSC isosurface plots showing the resolution ranges of the maps for the least favorable cross-sectional view (values refer to resolution). Arrow indicates the direction of preferred orientation (Z-resolution with respect to the electron beam). (**D**) Stereo views of the maps and models bound to the respective INSTIs highlighting the catalytic core.

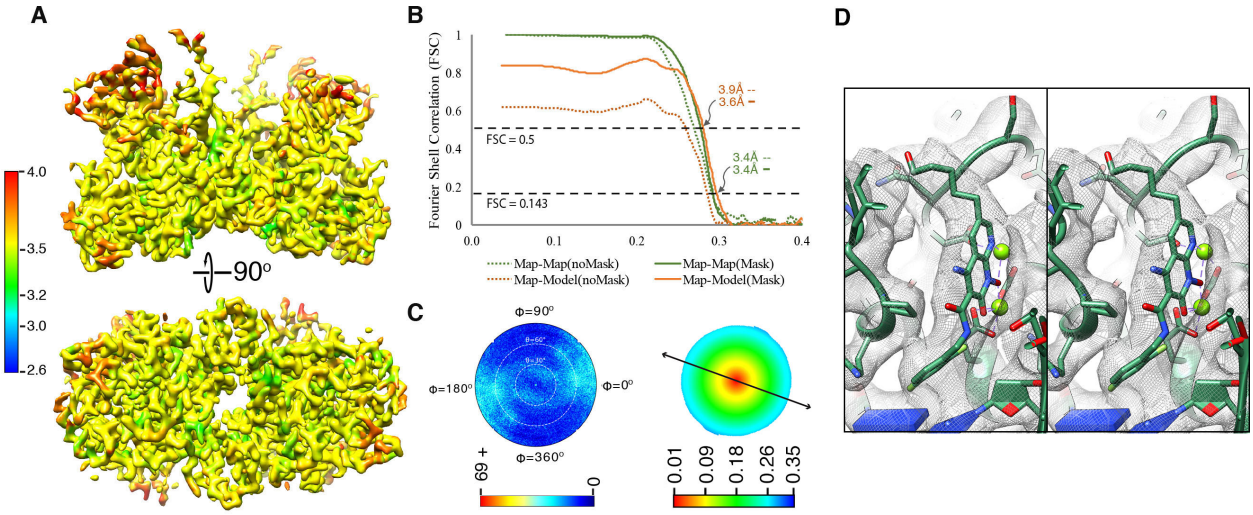

Figure S12. Cryo-EM structure determination and validation of compound 4c bound to the HIV CSC intasome. (**A**) Local resolution estimates for each map, colored in Chimera, accordingly. Side and bottom views of the reconstructions are shown. (**B**) FSC curves for half-map and map-to-model, both masked and unmasked, showing both FSC cutoffs 0.143 and 0.5. (**C**) Euler angle distribution plots describing the relative particle orientations contributing to the final refined maps (values refer to particle count) and the 3D FSC isosurface plots showing the resolution ranges of the map for the least favorable cross-sectional view (values refer to resolution). Arrow indicates the direction of preferred orientation (Z-resolution with respect to the electron beam). (**D**) Stereo views of the map and **4c** model highlighting the catalytic core where the drug binds.

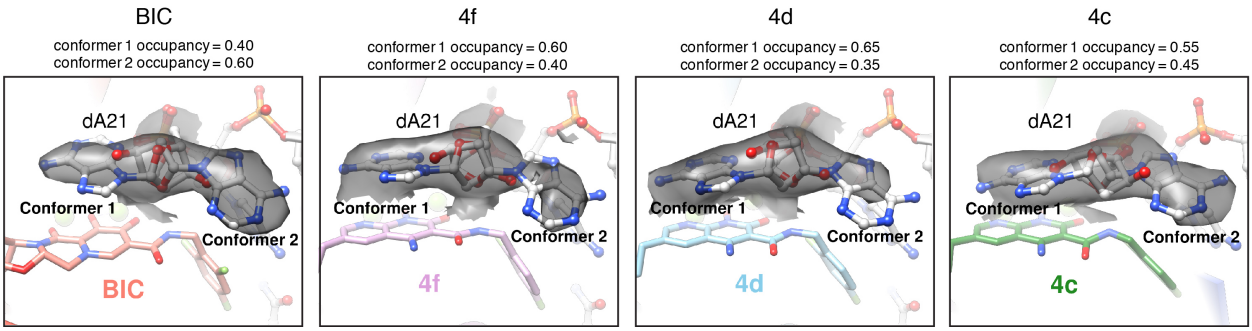

Fig. S13. Alternate rotameric configurations of the terminal 3′-adenosine. The terminal 3′-adenosine of the vDNA can adopt two alternative binding conformations in the presence of INSTIs. In rotamer 1, the adenine stacks on top of the bound INSTI and constructively contributes to INSTI binding. In rotamer 2, the adenine points away from the INSTI. Chemical optimization that promotes the stability of conformer 1 stability should be advantageous for ligand binding. The cryo-EM density map is contoured at 3.6 σ. Occupancy values were calculated by summing the average real space map values for the atoms (calculated in Chimera) comprising the base for each conformational state.

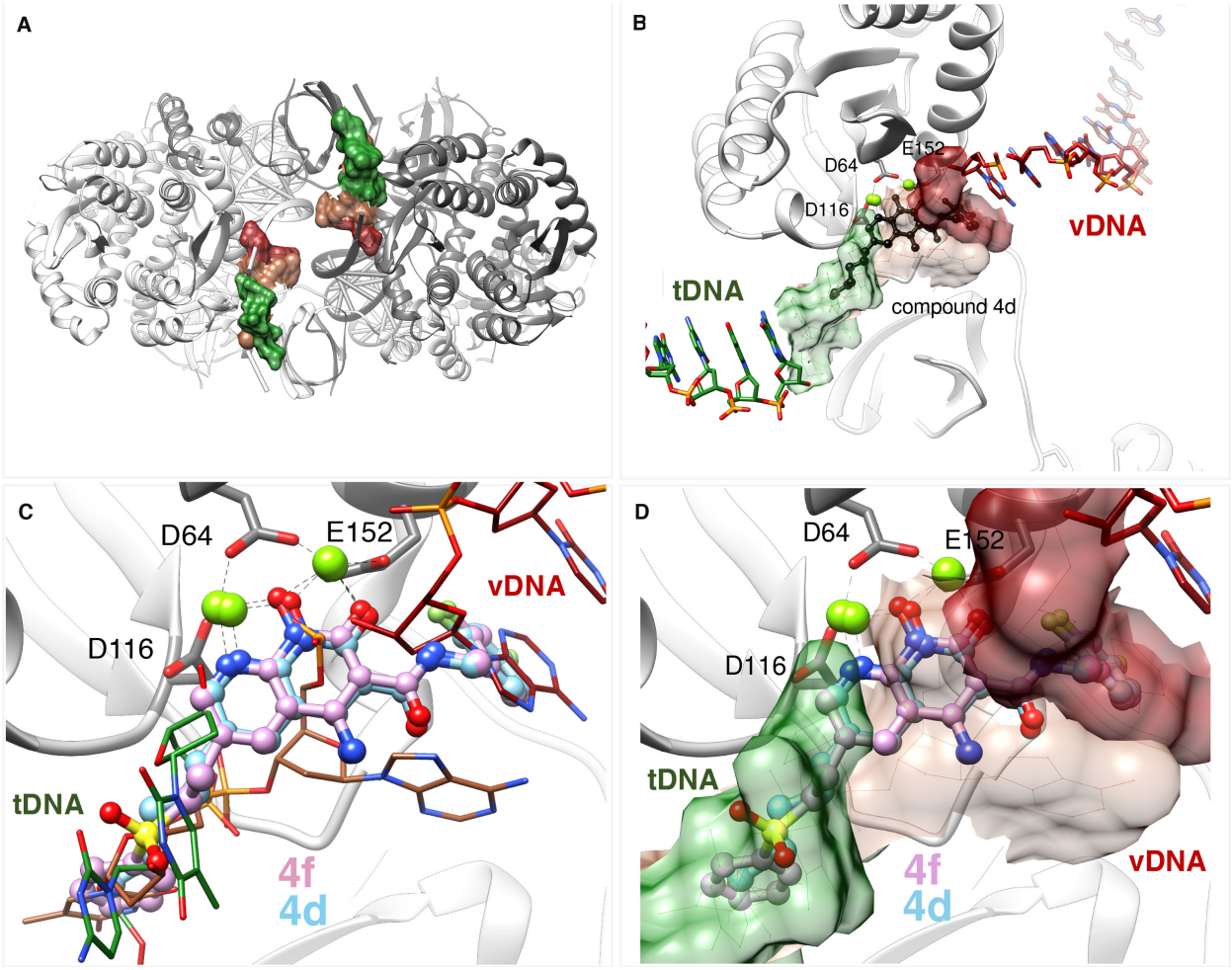

Fig. S14. Binding modes of compounds 4d and 4f follow the concept of filling the substrate envelope. The HIV intasome substrate envelope is shown as a multi-color surface/stick representation. It is generated from the post-3′-processed vDNA substrate from the HIV intasome (PDB 5U1C, dark red), the dinucleotide fragment of pre-3′-processed vDNA substrate from the PFV intasome (PDB 4E7I, light brown) and host target DNA substrate (PDB 5U1C, green). The same coloring scheme was used in all of the panels. (**A**) The HIV intasome is colored by asymmetric unit (grey and dark grey) and the substrate envelope is shown. (**B**) Active site region showing the conserved DDE motif and compound **4d** (black) bound completely within the substrate envelope. (**C**) Superposition of compounds **4d** (light blue) and **4f** (light pink) with substrate DNA fragments. For both **4d** and **4f** the terminal parts of their 6′ substituents occupy the

space where both vDNA and tDNA substrates bind. (**D**) Zoom on the fit of compounds **4d** (light blue) and **4f** (pink) within the substrate envelope.

.

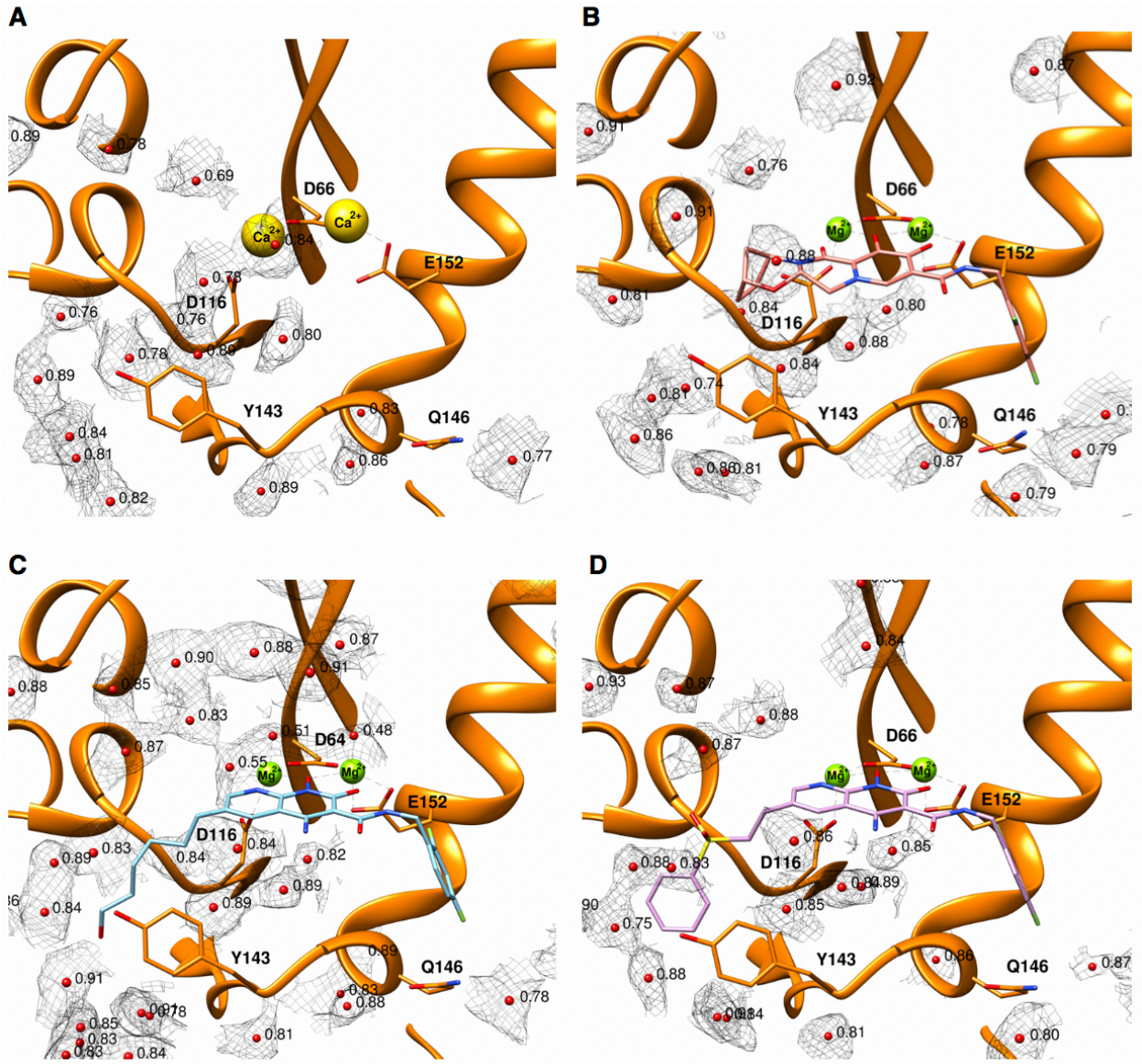

Fig. S15. Quantitative analysis of water molecules bound to HIV intasome maps. Zoom into the HIV intasome active sites of (**A**) apo, (**B**) **BIC**, (**C**) **4d,** and (**D**) **4f** bound structures, showing the solvent (O atoms from water) labeled by their calculated Q-scores (*43*). Density surrounding the water molecules of relative cryo-EM maps are shown.

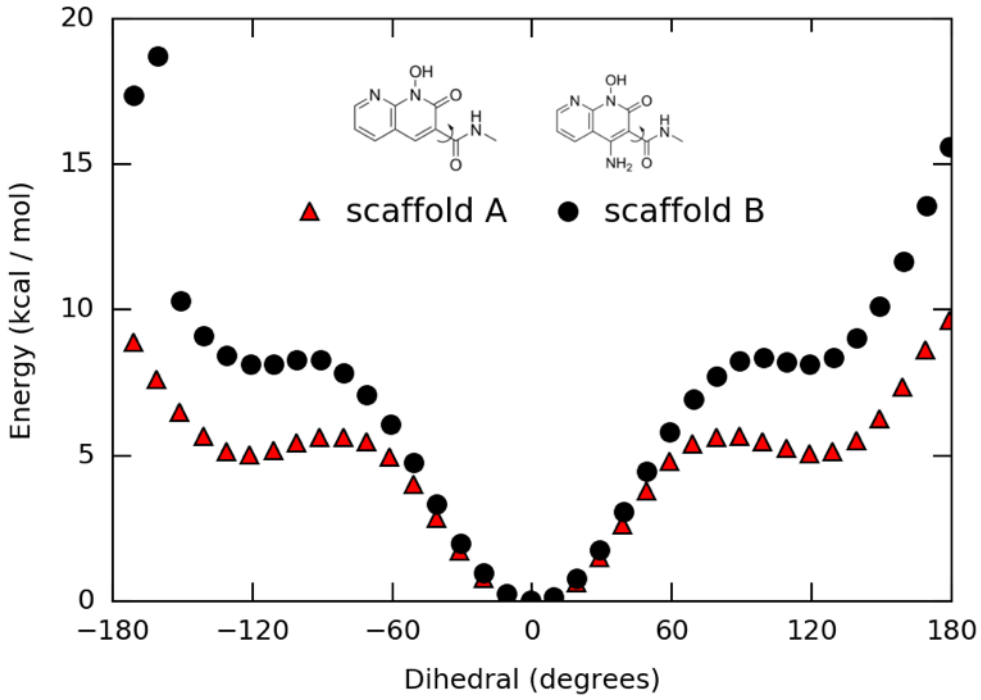

Fig. S16. The amino group in the naphthyridine scaffold helps to stabilize the structure of the bound-state rotamer. There is rotational freedom around the bond connecting the naphthyridine core to the amide linker (arrow in molecules). The bound state rotamer corresponds to a dihedral angle equal to 0 degrees, and is used as the reference energy (0 kcal/mol) in the torsion profile. In both scaffold A and B, the bound state rotamer is the most stable conformer. For conformers deviating from the bound state (i.e., a dihedral larger than 60 degrees), the addition of the amino group increases the energetic penalty from about 5 to 8 kcal/mol between scaffold A and B, respectively.

Data collection and processing	apo	BIC	4d	4f	4c
EMDB ID	**EMD-20481**	**EMD-20483**	**EMD-20484**	**EMD-20485**	**EMD-21038**
Microscope	Titan Krios	Titan Krios	Titan Krios	Titan Krios	Titan Krios
Detector	Gatan K2	Gatan K2	Gatan K2	Gatan K2	Gatan K2
Recording mode	Counting	Counting	Counting	Counting	Counting
Voltage (kV)	300	300	300	300	300
Magnification	37000	37000	37000	37000	37000
Tilts (20°,30°,40°; in %)	34,30,36	40,43,18	38,41,21	18,44,38	39,31,30
Total dose (e–/Å^2)	43	45	45	42	45
Dose rate (e–/pix/s)	5.4	5.6	5.6	5.3	5.6
Defocus range (μm)	1.5 - 3.0	1.5 - 3.0	1.5 - 3.0	1.5 - 3.0	1.5 - 3.0
Pixel size (Å)	0.79	0.79	0.79	0.79	0.79
Number of frames/movie (no.)	80	80	80	80	80
Frame rate (frames/sec)	10	10	10	10	10
Symmetry imposed	C2	C2	C2	C2	C2
Number of micrographs (no.)	1,989	2,188	2,024	2,072	2,783
Total picked particle (no.)	326,483	340,266	234,582	412,354	375,744
Particles used for final map (no.)	157,952	146,022	138,770	143,698	142,225
Resolution global (FSC 0.143, Å)	2.9	2.9	2.8	2.8	3.4
Resolution in CIC (FSC 0.143, Å)	2.7 – 3.7	2.7 – 3.7	2.6 – 3.6	2.7 – 3.6	3.1 – 4.3
SCF value*	0.87	0.87	0.85	0.83	0.87

Model statistics	apo	BIC	4d	4f	4c
PDB ID	**6PUT**	**6PUW**	**6PUY**	**6PUZ**	**6V3K**
Refinement package (Real space refinement)	Phenix	Phenix	Phenix	Phenix	Phenix
Model composition					
Protein (residues)	589	605	621	615	613
DNA (nucleotides)	34	36	36	36	36
Ligands	n/a	BIC	4d	4f	4c
Map CC	0.90	0.90	0.91	0.91	0.87
FSC map-to-model (global) (0.5)	3.0	3.0	3.0	3.0	3.6
RMSD [bonds] (Å)	0.007	0.005	0.011	0.007	0.006
RMSD [angles] (°)	0.820	0.582	0.831	0.809	0.706
All-atom clashscore	4.38	7.04	4.32	5.31	8.42
Molprobity score	1.31	1.42	1.39	1.32	1.79
Ramachandran plot					
Favored (%)	97.52	97.88	97.00	97.83	95.14
Allowed (%)	2.48	2.12	3.00	2.17	4.86
Outliers	0.00	0.00	0.00	0.00	0.00
Rotamer outliers (%)	0.2	0.2	0.2	0.2	0.2
CaBLAM outliers (%)	1.31	1.86	1.74	0.88	2.58
C-β deviations (%)	0	0	0	0	
EM-Ringer Score	4.56	4.70	4.33	4.50	3.33
Average B-factors					
protein (Å^2)	42.55	37.30	35.43	32.28	39.76
DNA (Å^2)	51.84	52.40	50.14	47.40	65.78
water (Å^2)	37.54	29.88	31.77	29.86	n/a
ligand (Å^2)	n/a	30.29	27.29	39.40	37.49

* The SCF value is calculated as described (*48*), but currently assumes that all orientations have been properly assigned and does not take into account false positive assignments

Table S1. Cryo-EM data collection and atomic modeling statistics

HIV-1	PFV	Chain	Resistance mutant
His51	Ile112	A	X
Val54	Pro115	A	
Gln62	Phe126	A	
Leu63	Ile127	A	
Asp64	Asp128	A	
Cys65	Tyr129	A	
Thr66	Ile130	A	X
His67	Gly131	A	
Leu68	Pro132	A	
Ile73	Val142	A	
Leu74	Leu143	A	X
Val75	Val144	A	
Glu92	Pro161	A	X
Thr115	Ser184	A	
Asp116	Asp185	A	
Asn117	Gln186	A	
Gly118	Gly187	A	X
Ser119	Ala188	A	
Asn120	Ala189	A	
Phe121	Phe190	A	
Thr122	Thr191	A	
Phe139	Phe208	A	
Gly140	Ser209	A	X
Ile141	Thr210	A	
Pro142	Pro211	A	
Tyr143	Tyr212	A	X
Asn144	His213	A	
Pro145	Pro214	A	
Gln146	Gln215	A	
Ser147	Ser216	A	X
Gln148	Ser217	A	X
Gly149	Gly218	A	X
Val150	Lys219	A	
Ile151	Val220	A	X
Glu152	Glu221	A	
Ser153	Arg222	A	X
Met154	Lys223	A	
Asn155	Asn224	A	X
Lys156	Ser225	A	
Lys159	Lys208	A	
Ser230	Ala328	K	X
Arg231	Arg329	K	
Arg263	Asp367	K	X
Lys264	Asn368	K	

Table S2. Conservation of residues near the active site between HIV-1 and PFV. Residues within 10 Å of **BIC** were identified and are indicated in the table, marked with the appropriate chain ID. The Dolutegravir bound PFV intasome was used for comparison (PDB 3S3M) (*17*). Green color indicates conserved residues between the two INs; red color indicates variable residues. "X" identifies residues that are prone to resistance (*12*) (https://hivdb.stanford.edu/dr-summary/resistance-notes/INSTI/).

References and Notes

1. A. R. Martin, R. F. Siliciano, Progress Toward HIV Eradication: Case Reports, Current Efforts, and the Challenges Associated with Cure. *Annu. Rev. Med.* **67**, 215–228 (2016). doi:10.1146/annurev-med-011514-023043 Medline

2. P. Lesbats, A. N. Engelman, P. Cherepanov, Retroviral DNA Integration. *Chem. Rev.* **116**, 12730–12757 (2016). doi:10.1021/acs.chemrev.6b00125

3. R. Craigie, F. D. Bushman, HIV DNA integration. *Cold Spring Harb. Perspect. Med.* **2**, a006890 (2012). doi:10.1101/cshperspect.a006890 Medline

4. D. O. Passos, M. Li, R. Yang, S. V. Rebensburg, R. Ghirlando, Y. Jeon, N. Shkriabai, M. Kvaratskhelia, R. Craigie, D. Lyumkis, Cryo-EM structures and atomic model of the HIV-1 strand transfer complex intasome. *Science* **355**, 89–92 (2017). doi:10.1126/science.aah5163 Medline

5. G. N. Maertens, S. Hare, P. Cherepanov, The mechanism of retroviral integration from X-ray structures of its key intermediates. *Nature* **468**, 326–329 (2010). doi:10.1038/nature09517 Medline

6. S. Hare, S. S. Gupta, E. Valkov, A. Engelman, P. Cherepanov, Retroviral intasome assembly and inhibition of DNA strand transfer. *Nature* **464**, 232–236 (2010). doi:10.1038/nature08784 Medline

7. A. Ballandras-Colas, D. P. Maskell, E. Serrao, J. Locke, P. Swuec, S. R. Jónsson, A. Kotecha, N. J. Cook, V. E. Pye, I. A. Taylor, V. Andrésdóttir, A. N. Engelman, A. Costa, P. Cherepanov, A supramolecular assembly mediates lentiviral DNA integration. *Science* **355**, 93–95 (2017). doi:10.1126/science.aah7002 Medline

8. A. Ballandras-Colas, M. Brown, N. J. Cook, T. G. Dewdney, B. Demeler, P. Cherepanov, D. Lyumkis, A. N. Engelman, Cryo-EM reveals a novel octameric integrase structure for betaretroviral intasome function. *Nature* **530**, 358–361 (2016). doi:10.1038/nature16955 Medline

9. Z. Yin, K. Shi, S. Banerjee, K. K. Pandey, S. Bera, D. P. Grandgenett, H. Aihara, Crystal structure of the Rous sarcoma virus intasome. *Nature* **530**, 362–366 (2016). doi:10.1038/nature16950 Medline

10. D. J. Hazuda, HIV integrase as a target for antiretroviral therapy. *Curr. Opin. HIV AIDS* **7**, 383–389 (2012). doi:10.1097/COH.0b013e3283567309 Medline

11. J. A. Grobler, D. J. Hazuda, Resistance to HIV integrase strand transfer inhibitors: In vitro findings and clinical consequences. *Curr. Opin. Virol.* **8**, 98–103 (2014). doi:10.1016/j.coviro.2014.07.006 Medline

12. K. Anstett, B. Brenner, T. Mesplede, M. A. Wainberg, HIV drug resistance against strand transfer integrase inhibitors. *Retrovirology* **14**, 36 (2017). doi:10.1186/s12977-017-0360-7 Medline

13. E. J. Arts, D. J. Hazuda, HIV-1 antiretroviral drug therapy. *Cold Spring Harb. Perspect. Med.* **2**, a007161 (2012). doi:10.1101/cshperspect.a007161 Medline

14. J. Riddell 4th, 2018 IAS-USA Recommendations for the Use of Antiretroviral Therapy for HIV: Building on Decades of Progress. *JAMA* **320**, 347–349 (2018). doi:10.1001/jama.2018.9184 Medline

15. P. A. Volberding, HIV Treatment and Prevention: An Overview of Recommendations From the IAS-USA Antiretroviral Guidelines Panel. *Top. Antivir. Med.* **25**, 17–24 (2017). Medline

16. S. Hare, A. M. Vos, R. F. Clayton, J. W. Thuring, M. D. Cummings, P. Cherepanov, Molecular mechanisms of retroviral integrase inhibition and the evolution of viral resistance. *Proc. Natl. Acad. Sci. U.S.A.* **107**, 20057–20062 (2010). doi:10.1073/pnas.1010246107 Medline

17. S. Hare, S. J. Smith, M. Métifiot, A. Jaxa-Chamiec, Y. Pommier, S. H. Hughes, P. Cherepanov, Structural and functional analyses of the second-generation integrase strand transfer inhibitor dolutegravir (S/GSK1349572). *Mol. Pharmacol.* **80**, 565–572 (2011). doi:10.1124/mol.111.073189 Medline

18. X. Z. Zhao, S. J. Smith, D. P. Maskell, M. Métifiot, V. E. Pye, K. Fesen, C. Marchand, Y. Pommier, P. Cherepanov, S. H. Hughes, T. R. Burke Jr., Structure-Guided Optimization of HIV Integrase Strand Transfer Inhibitors. *J. Med. Chem.* **60**, 7315–7332 (2017). doi:10.1021/acs.jmedchem.7b00596 Medline

19. X. Z. Zhao, S. J. Smith, D. P. Maskell, M. Metifiot, V. E. Pye, K. Fesen, C. Marchand, Y. Pommier, P. Cherepanov, S. H. Hughes, T. R. Burke Jr., HIV-1 Integrase Strand Transfer Inhibitors with Reduced Susceptibility to Drug Resistant Mutant Integrases. *ACS Chem. Biol.* **11**, 1074–1081 (2016). doi:10.1021/acschembio.5b00948 Medline

20. X. Z. Zhao, S. J. Smith, M. Métifiot, C. Marchand, P. L. Boyer, Y. Pommier, S. H. Hughes, T. R. Burke Jr., 4-amino-1-hydroxy-2-oxo-1,8-naphthyridine-containing compounds having high potency against raltegravir-resistant integrase mutants of HIV-1. *J. Med. Chem.* **57**, 5190–5202 (2014). doi:10.1021/jm5001908 Medline

21. M. Li, K. A. Jurado, S. Lin, A. Engelman, R. Craigie, Engineered hyperactive integrase for concerted HIV-1 DNA integration. *PLOS ONE* **9**, e105078 (2014). doi:10.1371/journal.pone.0105078 Medline

22. Y. Z. Tan, P. R. Baldwin, J. H. Davis, J. R. Williamson, C. S. Potter, B. Carragher, D. Lyumkis, Addressing preferred specimen orientation in single-particle cryo-EM through tilting. *Nat. Methods* **14**, 793–796 (2017). doi:10.1038/nmeth.4347 Medline

23. A. N. Engelman, P. Cherepanov, Retroviral intasomes arising. *Curr. Opin. Struct. Biol.* **47**, 23–29 (2017). doi:10.1016/j.sbi.2017.04.005 Medline

24. P. Rice, R. Craigie, D. R. Davies, Retroviral integrases and their cousins. *Curr. Opin. Struct. Biol.* **6**, 76–83 (1996). doi:10.1016/S0959-440X(96)80098-4 Medline

25. S. J. Smith, X. Z. Zhao, T. R. Burke Jr., S. H. Hughes, Efficacies of Cabotegravir and Bictegravir against drug-resistant HIV-1 integrase mutants. *Retrovirology* **15**, 37 (2018). doi:10.1186/s12977-018-0420-7 Medline

26. S. J. Smith, X. Z. Zhao, T. R. Burke Jr, S. H. Hughes, HIV-1 integrase inhibitors that are broadly effective against drug-resistant mutants. *Antimicrob. Agents Chemother.* **62**, e01035-18 (2018). doi:10.1128/AAC.01035-18 Medline

27. D. R. Langley, H. K. Samanta, Z. Lin, M. A. Walker, M. R. Krystal, I. B. Dicker, The terminal (catalytic) adenosine of the HIV LTR controls the kinetics of binding and dissociation of HIV integrase strand transfer inhibitors. *Biochemistry* **47**, 13481–13488 (2008). doi:10.1021/bi801372d Medline

28. S. J. Smith, G. T. Pauly, A. Akram, K. Melody, G. Rai, D. J. Maloney, Z. Ambrose, C. J. Thomas, J. T. Schneider, S. H. Hughes, Rilpivirine analogs potently inhibit drug-resistant HIV-1 mutants. *Retrovirology* **13**, 11 (2016). doi:10.1186/s12977-016-0244-2 Medline

29. N. M. King, M. Prabu-Jeyabalan, E. A. Nalivaika, C. A. Schiffer, Combating susceptibility to drug resistance: Lessons from HIV-1 protease. *Chem. Biol.* **11**, 1333–1338 (2004). doi:10.1016/j.chembiol.2004.08.010 Medline

30. M. N. L. Nalam, A. Ali, G. S. K. K. Reddy, H. Cao, S. G. Anjum, M. D. Altman, N. K. Yilmaz, B. Tidor, T. M. Rana, C. A. Schiffer, Substrate envelope-designed potent HIV-1 protease inhibitors to avoid drug resistance. *Chem. Biol.* **20**, 1116–1124 (2013). doi:10.1016/j.chembiol.2013.07.014 Medline

31. N. Kurt Yilmaz, R. Swanstrom, C. A. Schiffer, Improving Viral Protease Inhibitors to Counter Drug Resistance. *Trends Microbiol.* **24**, 547–557 (2016). doi:10.1016/j.tim.2016.03.010 Medline

32. C. Suloway, J. Pulokas, D. Fellmann, A. Cheng, F. Guerra, J. Quispe, S. Stagg, C. S. Potter, B. Carragher, Automated molecular microscopy: The new Leginon system. *J. Struct. Biol.* **151**, 41–60 (2005). doi:10.1016/j.jsb.2005.03.010 Medline

33. S. Q. Zheng, E. Palovcak, J.-P. Armache, K. A. Verba, Y. Cheng, D. A. Agard, MotionCor2: Anisotropic correction of beam-induced motion for improved cryo-electron microscopy. *Nat. Methods* **14**, 331–332 (2017). doi:10.1038/nmeth.4193 Medline

34. G. C. Lander, S. M. Stagg, N. R. Voss, A. Cheng, D. Fellmann, J. Pulokas, C. Yoshioka, C. Irving, A. Mulder, P.-W. Lau, D. Lyumkis, C. S. Potter, B. Carragher, Appion: An integrated, database-driven pipeline to facilitate EM image processing. *J. Struct. Biol.* **166**, 95–102 (2009). doi:10.1016/j.jsb.2009.01.002 Medline

35. T. Grant, N. Grigorieff, Measuring the optimal exposure for single particle cryo-EM using a 2.6 Å reconstruction of rotavirus VP6. *elife* **4**, e06980 (2015). doi:10.7554/eLife.06980 Medline

36. D. Tegunov, P. Cramer, Real-time cryo-electron microscopy data preprocessing with Warp. *Nat. Methods* **16**, 1146–1152 (2019). doi:10.1038/s41592-019-0580-y Medline

37. T. Grant, A. Rohou, N. Grigorieff, cisTEM, user-friendly software for single-particle image processing. *elife* **7**, e35383 (2018). doi:10.7554/eLife.35383 Medline

38. P. D. Adams, P. V. Afonine, G. Bunkóczi, V. B. Chen, I. W. Davis, N. Echols, J. J. Headd, L.-W. Hung, G. J. Kapral, R. W. Grosse-Kunstleve, A. J. McCoy, N. W. Moriarty, R. Oeffner, R. J. Read, D. C. Richardson, J. S. Richardson, T. C. Terwilliger, P. H. Zwart,

PHENIX: A comprehensive Python-based system for macromolecular structure solution. *Acta Cryst.* **D66**, 213–221 (2010). doi:10.1107/S0907444909052925 Medline

39. M. Hohn, G. Tang, G. Goodyear, P. R. Baldwin, Z. Huang, P. A. Penczek, C. Yang, R. M. Glaeser, P. D. Adams, S. J. Ludtke, SPARX, a new environment for Cryo-EM image processing. *J. Struct. Biol.* **157**, 47–55 (2007). doi:10.1016/j.jsb.2006.07.003 Medline

40. P. Emsley, B. Lohkamp, W. G. Scott, K. Cowtan, Features and development of Coot. *Acta Cryst.* **D66**, 486–501 (2010). doi:10.1107/S0907444910007493 Medline

41. N. W. Moriarty, R. W. Grosse-Kunstleve, P. D. Adams, electronic Ligand Builder and Optimization Workbench (eLBOW): A tool for ligand coordinate and restraint generation. *Acta Cryst.* **D65**, 1074–1080 (2009). doi:10.1107/S0907444909029436 Medline

42. A. W. Schüttelkopf, D. M. F. van Aalten, PRODRG: A tool for high-throughput crystallography of protein-ligand complexes. *Acta Cryst.* **D60**, 1355–1363 (2004). doi:10.1107/S0907444904011679 Medline

43. G. Pintilie, K. Zhang, Z. Su, S. Li, M. F. Schmid, W. Chiu, Measurement of Atom Resolvability in CryoEM Maps with Q-scores. bioRxiv 722991 [Preprint]. 5 August 2019. https://doi.org/10.1101/722991

44. V. B. Chen, W. B. Arendall 3rd, J. J. Headd, D. A. Keedy, R. M. Immormino, G. J. Kapral, L. W. Murray, J. S. Richardson, D. C. Richardson, MolProbity: All-atom structure validation for macromolecular crystallography. *Acta Cryst.* **D66**, 12–21 (2010). doi:10.1107/S0907444909042073 Medline

45. E. F. Pettersen, T. D. Goddard, C. C. Huang, G. S. Couch, D. M. Greenblatt, E. C. Meng, T. E. Ferrin, UCSF Chimera—A visualization system for exploratory research and analysis. *J. Comput. Chem.* **25**, 1605–1612 (2004). doi:10.1002/jcc.20084 Medline

46. E. Krissinel, K. Henrick, Secondary-structure matching (SSM), a new tool for fast protein structure alignment in three dimensions. *Acta Cryst.* **D60**, 2256–2268 (2004). doi:10.1107/S0907444904026460 Medline

47. S. J. Smith, S. H. Hughes, Rapid screening of HIV reverse transcriptase and integrase inhibitors. *J. Vis. Exp.* **86**, e51400 (2014). doi:10.3791/51400 Medline

48. P. R. Baldwin, D. Lyumkis, Non-Uniformity of Projection Distributions Attenuates Resolution in Cryo-EM. *Prog. Biophys. Mol. Biol.* **150**, 160–183 (2020). doi:10.1016/j.pbiomolbio.2019.09.002 Medline